

Eur. Phys. J. A (2014) 50: 48

DOI 10.1140/epja/i2014-14048-3

## Electroweak measurements of neutron densities in CREX and PREX at JLab, USA

C.J. Horowitz, K.S. Kumar and R. Michaels



Società  
Italiana  
di Fisica



Springer

# Electroweak measurements of neutron densities in CREX and PREX at JLab, USA<sup>\*</sup>

C.J. Horowitz<sup>1</sup>, K.S. Kumar<sup>2</sup>, and R. Michaels<sup>3,a</sup>

<sup>1</sup> Indiana University, Bloomington, Indiana, USA

<sup>2</sup> University of Massachusetts, Amherst, Massachusetts, USA

<sup>3</sup> Thomas Jefferson National Accelerator Facility, Newport News, VA, USA

Received: 11 July 2013 / Revised: 18 September 2013

Published online: 27 February 2014 – © Società Italiana di Fisica / Springer-Verlag 2014

Communicated by Z.-E. Meziani

**Abstract.** Measurement of the parity-violating electron scattering asymmetry is an established technique at Jefferson Lab and provides a new opportunity to measure the weak charge distribution and hence pin down the neutron radius in nuclei in a relatively clean and model-independent way. This is because the  $Z$  boson of the weak interaction couples primarily to neutrons. We will describe the PREX and CREX experiments on  $^{208}\text{Pb}$  and  $^{48}\text{Ca}$ , respectively; these are both doubly magic nuclei whose first excited state can be discriminated by the high-resolution spectrometers at JLab. The heavier lead nucleus, with a neutron excess, provides an interpretation of the neutron skin thickness in terms of properties of bulk neutron matter. For the lighter  $^{48}\text{Ca}$  nucleus, which is also rich in neutrons, microscopic nuclear theory calculations are feasible and are sensitive to poorly constrained 3-neutron forces.

## 1 Introduction

Precise measurements of neutron densities provide a powerful probe of the symmetry energy  $S$ . If  $S$  increases with density, this will help move extra neutrons, in a neutron rich nucleus, from the high density interior into the low-density surface region and create a neutron-rich skin. Therefore, measuring the thickness of this neutron skin allows one to infer the density dependence of the symmetry energy [1, 2]; see also the contribution to this topical issue by Vinãs *et al.* [3].

The neutron skin thickness  $\Delta R_{np}$  is the difference in r.m.s. neutron  $R_n$  and proton  $R_p$  radii,

$$\Delta R_{np} = R_n - R_p. \quad (1)$$

In light nuclei with  $N \approx Z$ , the neutrons and protons have similar density distributions. With increasing neutron number, the radius of the neutron density distribution becomes larger than that of the protons, reflecting the pressure from the symmetry energy.

Proton radii have been determined accurately for many nuclei using electron scattering experiments [4–6]. This accuracy reflects the accuracy of perturbative treatments of the electromagnetic process. The neutron density

distribution is more difficult to measure accurately because it interacts mainly with hadronic probes (pions [7], protons [8–10], antiprotons [11, 12], and alphas [13, 14]) through nonperturbative interactions, the theoretical description of which is model-dependent. Other approaches to inferring  $R_n$  include inelastic scattering excitation of giant dipole resonances [15–17] and atomic mass fits [18, 19]. Neutron radii can also be measured with neutrino-nucleus elastic scattering [20, 21]. Furthermore, new methods to detect low-energy nuclear recoils will likely lead to important advances in neutrino scattering technology. However, systematic errors may limit the precision of neutrino measurements of neutron radii.

Parity-violation electron scattering, which arises from the weak interaction, provides a theoretically clean method to measure neutron radii  $R_n$ . This is because the weak charge of a neutron is much larger than that of a proton. Therefore, the  $Z^0$  boson, that mediates the weak neutral current, couples primarily to neutrons. As a result, parity violation provides a model independent way to locate neutrons inside a nucleus, see sect. 2. Parity-violating experiments are difficult because the measured asymmetry,  $A_{PV}$ ,

$$A_{PV} = \frac{\sigma_R - \sigma_L}{\sigma_R + \sigma_L}, \quad (2)$$

where  $\sigma_{R(L)}$  is the cross section for right (left)-handed helicity of the incident electrons, is very small, of order one part per million (ppm).

<sup>\*</sup> Contribution to the Topical Issue “Nuclear Symmetry Energy” edited by Bao-An Li, Àngels Ramos, Giuseppe Verde, Isaac Vidaña.

<sup>a</sup> e-mail: rom@jlab.org

Recently, the Lead Radius Experiment (PREX) at Jefferson Laboratory has pioneered parity-violating measurements of neutron radii and demonstrated excellent control of systematic errors [22]. The experimental configuration for PREX is similar to that used previously for studies of the weak form factor of the proton and  $^4\text{He}$  [23–27]. The Thomas Jefferson National Accelerator Facility provided excellent beam quality, while the large spectrometers in Hall A allowed PREX to separate elastically and inelastically scattered electrons and to greatly reduce backgrounds.

This paper is organized as follows. In sect. 2 we describe the formalism for parity-violating measurements of neutron densities, which has been published in refs. [28, 29]. The experimental methods are explained in sect. 3, adapted from refs. [23–28] but containing some previously unpublished details. The success of the methods was demonstrated by the PREX experiment on  $^{208}\text{Pb}$ , discussed in sect. 4 based on [22]. The main new material is the discussion of a planned follow-on measurement PREX-II [30] in sect. 4 and the CREX proposal for  $^{48}\text{Ca}$  [31] in sect. 5, with an outlook based on the recent CREX workshop [32]. These experiments PREX-II and CREX should measure neutron skins with high accuracy. We conclude in sect. 6.

## 2 Parity-violating measurements of neutron densities

In the Born approximation, the parity-violating cross-section asymmetry for longitudinally polarized electrons elastically scattered from an unpolarized nucleus,  $A_{PV}$ , is

$$A_{PV} \approx -\frac{G_F Q^2 Q_W}{4\pi\alpha\sqrt{2}Z} \frac{F_W(Q^2)}{F_{ch}(Q^2)}, \quad (3)$$

where  $G_F$  is the Fermi constant,  $\alpha$  the fine structure constant, and  $F_{ch}(Q^2)$  is the Fourier transform of the known charge density. The asymmetry is proportional to the weak form factor  $F_W(Q^2)$ . This is closely related to the Fourier transform of the neutron density (see below), and therefore the neutron density can be extracted from an electro-weak measurement [33].

However, the Born approximation is not valid for a heavy nucleus and Coulomb-distortion effects must be included. These have been accurately calculated [34] because the charge density is well known, and many other details relevant for a practical parity-violation experiment to measure neutron densities have been discussed in a previous publication [28].

The weak form factor is the Fourier transform of the weak charge density  $\rho_W(r)$ ,

$$F_W(Q^2) = \frac{1}{Q_W} \int d^3r \frac{\sin Qr}{Qr} \rho_W(r), \quad (4)$$

and is normalized  $F(Q=0) = 1$ . The total weak charge of the nucleus is  $Q_W = \int d^3r \rho_W(r)$ . For  $\rho_W(r)$  of a spin-zero nucleus, we neglect meson exchange and spin-orbit

currents and write [28]

$$\rho_W(r) = 4 \int d^3r' [G_n^Z(|\mathbf{r}-\mathbf{r}'|)\rho_n(r') + G_p^Z(|\mathbf{r}-\mathbf{r}'|)\rho_p(r')]. \quad (5)$$

Here the density of weak charge in a single proton  $G_p^Z(r)$  or neutron  $G_n^Z(r)$  is the Fourier transform of the nucleon (Electric) Sachs form factors  $G_p^Z(Q^2)$  and  $G_n^Z(Q^2)$ . These describe the coupling of a  $Z^0$  boson to a proton or neutron [28],

$$4G_p^Z = q_p G_E^p + q_n G_E^n - G_E^s, \quad (6)$$

$$4G_n^Z = q_n G_E^p + q_p G_E^n - G_E^s. \quad (7)$$

At tree level, the weak nucleon charges are  $q_n^0 = -1$  and  $q_p^0 = 1 - 4\sin^2\Theta_W$ . We include radiative corrections by using the values  $q_n = -0.9878$  and  $q_p = 0.0721$  based on the up  $C_{1u}$  and down  $C_{1d}$  quark weak charges in refs. [35, 36]. The Fourier transform of the proton (neutron) electric form factor is  $G_E^p(r)$  ( $G_E^n(r)$ ) and has total charge  $\int d^3r G_E^p(r) = 1$  ( $\int d^3r G_E^n(r) = 0$ ). Finally  $G_E^s$  describes strange quark contributions to the nucleon's electric form factor [23–27, 37–45].

Given that  $q_p$  is small, and strange quark contributions have been greatly limited by previous measurements, we see that  $\rho_W(r)$  is primarily the point neutron density  $\rho_n(r)$  folded with the weak form factor of a single neutron. The neutron density is normalized to the number of neutrons  $\int d^3r \rho_n(r) = N$ , while the proton density is normalized to the number of protons  $\int d^3r \rho_p(r) = Z$ . The point neutron radius  $R_n$  is defined from  $R_n^2 = \int d^3r r^2 \rho_n(r)/N$ .

Measuring  $A_{PV}$  for a single low  $Q^2$  allows one to infer  $F_W(Q^2)$  and from it the r.m.s. weak radius  $R_W$ . This is then related to  $R_n$  [29],

$$R_n^2 = \frac{Q_W}{q_n N} R_W^2 - \frac{q_p Z}{q_n N} R_{ch}^2 - \langle r_p^2 \rangle - \frac{Z}{N} \langle r_n^2 \rangle + \frac{Z+N}{q_n N} \langle r_s^2 \rangle. \quad (8)$$

Here the (known) charge radius of the nucleus is  $R_{ch}$ , the square of the charge radius of a single proton is  $\langle r_p^2 \rangle = 0.769 \text{ fm}^2$  and that of a single neutron is  $\langle r_n^2 \rangle = -0.116 \text{ fm}^2$ , finally  $\langle r_s^2 \rangle = \int d^3r' r'^2 G_E^s(r')$  is the square of the nucleon strangeness radius. Previous measurements [23–27, 37–45] have constrained this to be small. Note that the  $-\langle r_p^2 \rangle$  term in eq. (8) comes from the weak radius of a single neutron. This is related to the charge radius of a single proton.

To summarize this section, measuring  $A_{PV}$  determines the weak form factor  $F_W(Q^2)$  and from this the neutron radius  $R_n$ . The neutron skin thickness  $R_n - R_p$  then follows, since  $R_p$  is known. Finally, the neutron skin thickness constrains the density dependence of the symmetry energy.

## 3 Experimental method

### 3.1 Overview of the method

The experiments run at Jefferson Lab using the high-resolution spectrometers (HRS) [46] in Hall A, comprising

a pair of 3.7msr spectrometer systems with  $10^{-4}$  momentum resolution, which focus elastically scattered electrons onto total-absorption detectors in their focal planes. The “hardware momentum resolution” of the spectrometer system, *i.e.* the width of the distribution for monoenergetic electrons with no event-by-event corrections, is better than  $10^{-3}$ , so that the elastic electrons populate a region that is otherwise free from contamination from inelastic events.

A polarized electron beam scatters from a target foil, and ratios of detected flux to beam current integrated in the helicity period are formed (so-called “flux integration”), and the parity-violating asymmetry in these ratios computed from the helicity-correlated difference divided by the sum (eq. (2)). Separate studies at lower rates are required to measure backgrounds, acceptance, and  $Q^2$ . Polarization is measured once a day by a Møller polarimeter, and monitored continuously with the Compton polarimeter.

The asymmetry is small, of the order of one or two parts per million (ppm) for the kinematics of interest for the two nuclei under primary consideration namely,  $^{208}\text{Pb}$  (PREX) and  $^{48}\text{Ca}$  (CREX). To have significant impact on our knowledge of skin thicknesses,  $A_{PV}$  must be measured with a precision in the range of 3% or better (see fig. 4). Experiments of this nature are optimized to the challenges of precision measurement of very small asymmetries, which require high count rates and low noise to achieve statistical precision as well as a careful regard for potential systematic errors associated with helicity reversal, which must be maintained below the  $10^{-8}$  level (see sect. 3.2).

One common feature of all measurements of parity violation in electron scattering is a rapid flipping of the electron beam helicity, allowing a differential measurement between opposing polarization states on a short timescale. The enabling technology for these measurements lies in the semiconductor photo-emission polarized electron source, which allows rapid reversal of the electron polarization while providing high luminosity, high polarization, and a high degree of uniformity between the two beam helicity states. Developments with the polarized source at Jefferson Lab are critical to the success of this program [47,48].

In a parity experiment, the asymmetry generally increases with  $Q^2$  while the cross section decreases, which leads to an optimum choice of kinematics. For parity-violating neutron density experiments, the optimum kinematics is the point which effectively minimizes the error in the neutron radius  $R_n$ . This is equivalent to maximizing the following product, which is the figure of merit (FOM),

$$FOM = R \times A^2 \times \epsilon^2. \quad (9)$$

Here,  $R$  is the scattering rate,  $A$  is the asymmetry,  $\epsilon = \frac{dA/A}{dR_n/R_n}$  is the sensitivity of the asymmetry for a small change in  $R_n$ ,  $dR_n/R_n$  is a fractional change in  $R_n$  and  $dA/A$  is a corresponding fractional change in  $A$ . Note that the FOM defined for many types of parity-violation experiments is  $R \times A^2$ , but the neutron-density measurements must also fold in the sensitivity  $\epsilon$ .

Given practical constraints on the solid angle of the HRS, the optimization algorithm favors smaller scattering angles. Using septum magnets we reach  $\sim 5^\circ$  scattering angle. Once the angle is fixed, the optimum energy for elastic scattering can be specified. Simulations that are performed to design the experiment include the Coulomb distortions, as well as radiative losses, multiple scattering, and ionization losses in materials, together with a model for the tracking of particle trajectories through the HRS and septum magnets.

The two nuclei of interest for 1%, or better,  $R_n$  measurements ( $^{48}\text{Ca}$  and  $^{208}\text{Pb}$ ) are equally accessible experimentally and have been very well studied [4,49–52]. These are doubly magic and have a simple nuclear structure, making them good candidates for extracting the symmetry energy. Each nucleus has the advantage that it has a large splitting to the first excited state (2.60 MeV for  $^{208}\text{Pb}$  and 3.84 MeV for  $^{48}\text{Ca}$ ), thus lending themselves well to the use of a flux integration technique.

### 3.2 Control of random and systematic fluctuations

To achieve the  $10^{-8}$  statistical precision and systematic control for  $A_{PV}$  measurements requires a precise control and evaluation of systematic errors, as has been developed at Jefferson Lab [23–27] and elsewhere [53]. The apparatus must have the ability of measuring rates in excess of 1 GHz with negligible deadtime. In this section we will discuss some of the details of the techniques involved.

The polarized electron beam originates from a strained GaAsP photocathode illuminated by circularly polarized light [47, 48]. Several monitoring devices measure the beam’s intensity, energy, polarization. The sign of the laser circular polarization determines the electron helicity; this is held constant for periods of typically 8 ms, referred to as “windows”. The integrated responses of detector PMTs and beam monitors are digitized by an 18-bit ADC and recorded for each window. The helicity states are arranged in patterns, for example (+ – – + or – + + –) for a quadruplet structure with each window 8.23 ms long. These patterns ensure that complementary measurements are made at the same phase relative to the 60 Hz line power, thus canceling power-line noise from the asymmetry measurement.

The signals are integrated over the helicity window because the rates are too high for a counting DAQ. The right-left helicity asymmetry in the integrated detector response, normalized to the beam intensity, is computed for sets of complementary helicity windows in each quadruplet to form the raw asymmetry  $A_{raw}$ . The sequence of these patterns is chosen with a pseudo-random number generator. The reversals of the beam helicity occur in a random sequence in order to uncouple them from other parameters which affect the cross section. To take full advantage of the high scattered flux and to ensure that  $A_{raw}$  measurement fluctuations are dominated by counting statistics, the electronics chain is designed to be capable of measuring the response of each helicity window with a precision better than  $10^{-4}$ .

The requirement of high statistics also requires high current on a relatively thick target. For the case of PREX, an isotopically pure  $^{208}\text{Pb}$  0.55 mm thick target is used. Two  $150\ \mu\text{m}$  diamond foils sandwich the lead foil to improve thermal conductance to a copper frame cooled to 20 K with cryogenic helium. Nonuniformities in target thickness due to thermal damage could cause window-to-window luminosity fluctuations from variations in the target area sampled by the rastered beam. This potential source of random noise is controlled by locking the raster pattern frequency to a multiple of the helicity frequency. Low-current calibration data, triggered on individual scattered electrons, are regularly collected to evaluate the thickness of lead relative to diamond.

The sensitivity of the cross section to fluctuations in the beam parameters, as well as the helicity correlated differences in them must be accurately monitored concomitant with the collection of physics data. Care must be taken to isolate the helicity signals, since electronic pickup of the helicity correlated signals could cause a false asymmetry. For an integrating DAQ system, the linearity of the detector electronics and the susceptibility to backgrounds are important issues. The particle detectors for the scattered electrons are quartz<sup>1</sup> bars. Cherenkov light from each quartz bar traverse air light guides and are detected by photo-multipliers (PMT).

While a quartz Cherenkov detector is valued for radiation hardness and insensitivity to soft backgrounds, there is a particular challenge for electrons with energy less than 2 GeV. In this energy range, shower fluctuations in a thick or radiated detector significantly degrade energy resolution, while photon statistics degrade the energy resolution for a thin detector. The energy resolution  $\Delta E$  at nominal electron energy  $E$  increases the statistical error that one would have with infinite resolution  $\sigma_0$  to obtain the total statistical error  $\sigma = \sigma_0 \sqrt{1 + (\frac{\Delta E}{E})^2}$ . During PREX-I, the detector thickness was optimized and achieved sufficient energy resolution so that the statistical degradation factor was 1.06.

To study and help cancel the helicity-correlated systematics, there should be more than one way to change the sign of the beam helicity. A half-wave ( $\lambda/2$ ) plate was periodically inserted into the injector laser optical path, reversing the sign of the electron beam polarization relative to both the electronic helicity control signals and the voltage applied to the polarized source laser electro-optics. Roughly equal statistics were collected with this wave plate inserted and retracted, suppressing many possible sources of systematic error.

An independent method of helicity reversal was feasible with a pair of Wien spin-rotators separated by a solenoid, providing an additional powerful check of systematic control. Reversing the direction of the solenoidal field reversed the electron beam helicity while the beam optics, which depend on the square of the solenoidal magnetic field, were unchanged. The  $\lambda/2$  reversal was done

<sup>1</sup> Artificial fused silica, brand name Spectrosil 2000 from Quartz Plus, Inc.

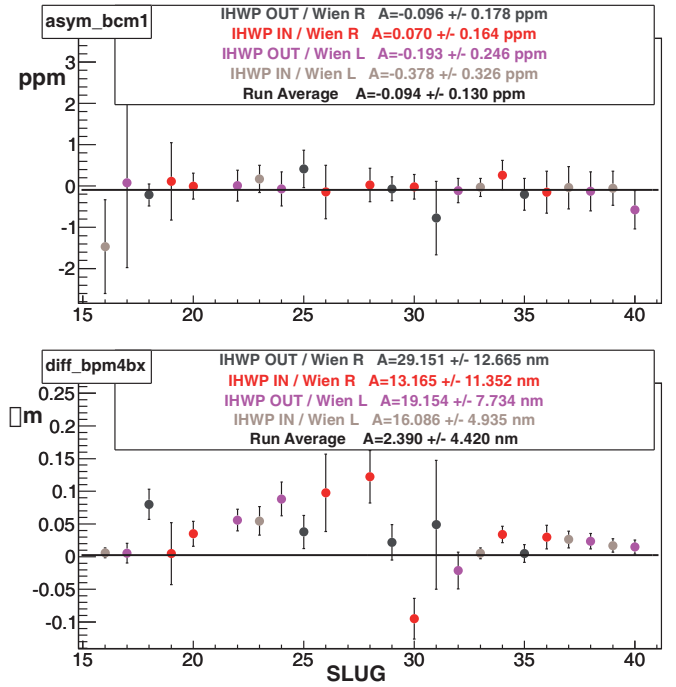


**Fig. 1.** PREX-I helicity-correlated charge asymmetries (top) and position differences (bottom) on a representative monitor versus slug (a slug is  $\sim 1$  day of running). The different colors correspond to four different combinations of IHWP and Wien used for slow sign reversal, as explained in the text. To illustrate the systematics, the data points are plotted without sign correction for the helicity flip. The final average with all sign corrections is shown by the black horizontal bar and was controlled at the 5 nm level averaged over the PREX-I run. The charge asymmetry was forced to zero by the standard feedback system.

about every 12 hours and the magnetic spin reversal was performed every few days. The dataset consisting of a period between two successive  $\lambda/2$  or magnetic spin-reversals is referred to as a “slug”.

### 3.3 Beam-induced asymmetries

PREX-I was able to achieve overall asymmetry corrections due to helicity-correlated beam position fluctuations of about 40 ppb with position differences  $< 5$  nm. The position/asymmetry correlations are measured using two independent methods: first, directly observing the asymmetry correlations by the natural beam motion and second, by systematically perturbing the beam through a set of magnetic coils (dithering). Achieving these small values for the differences was possible in part by periodically inserting the half-wave plate in the injector and flipping the helicity of the beam using a double-Wien filter which helps them cancel over time. Figure 1 shows the helicity-correlated charge asymmetries and position differences *versus* time during PREX-I. A beam current monitor (BCM) and one representative beam position monitor (BPM) is shown; the other BPMs look similar. Feedback on the charge

asymmetry forced it to be zero within 0.13 ppm. The utility of the slow reversals is demonstrated the BPM difference plot; without them, the position differences remained at the  $\sim 50$  nm level (the points without sign correction) averaged over the experiment; with the reversals, the differences averaged to the  $\sim 5$  nm level (the black lines) and became a negligible correction [54–58].

The correction made for PREX-I was dominated by fluctuations in the scattered beam intensity due to small changes in the accepted angle and the sharply falling lead cross section. CREX will run at a higher  $Q^2$  ( $0.022$   $(\text{GeV}/c)^2$ ), and since  $^{48}\text{Ca}$  is a smaller nucleus,  $\frac{d\sigma}{d\theta}/\sigma$  is smaller by a factor of 4.3. We conservatively estimate that the uncertainty on the corrections for CREX will be  $\sim 7$  ppb, the same as for PREX-I.

The integrated signals in the helicity windows are normalized to the beam current monitor signals to remove helicity-correlated beam intensity fluctuations. Nonlinearities in the BCMs produce additional false asymmetries, which are related to the overall charge asymmetry. Based on past running, we can expect an accumulated charge asymmetry less than 100 ppb and an uncertainty on that correction of 1.5%, so 1.5 ppb, or 0.1% propagated to the final asymmetry.

### 3.4 Contributions from inelastic states and isotopes

While doubly magic nuclei are preferred for their simple theoretical structure, they are also preferred experimentally because they have a large energy separation between elastic scattering and the first excited levels, as mentioned in sect. 3.1. For  $^{208}\text{Pb}$  ( $^{48}\text{Ca}$ ) the separation is 2.60 (3.84) MeV. Using the HRS spectrometers with  $10^{-3}$  hardware momentum resolution, we can place the elastic peak on our detectors, while ensuring that the inelastic electrons are not intercepted.

In ref. [28] the asymmetry for the 2.60 MeV  $3^-$  state of  $^{208}\text{Pb}$  was calculated using a model of collective nuclear excitations, assumed to be isoscalar, and found to be comparable to the elastic asymmetry, with the result  $A(3^-) \approx 1.25A_{\text{elastic}}$  and a relative uncertainty of 35% mainly due to unknown Coulomb distortions. In PREX, the relative rates of inelastic electrons were measured with a thin lead target in counting mode [54]. The first state was at the edge of our detector acceptance, and the rate multiplied by the acceptance was  $< 4 \times 10^{-4}$ . Higher excited states were even further away from our detector and their rates were negligible [54].

The lead is 99.1% pure  $^{208}\text{Pb}$  with 0.7% of  $^{207}\text{Pb}$ , 0.2% of  $^{206}\text{Pb}$ , and negligible amounts ( $< 10^{-4}$ ) of other elements. The  $^{48}\text{Ca}$  target is 99% chemically pure and the only important isotope contamination is a 3% contamination from  $^{40}\text{Ca}$ . We have evaluated the amount of inelastic  $^{48}\text{Ca}$  contamination based on form factor measurements of electron scattering [49] which covered the same momentum transfer range of CREX. Elastic and inelastic events were simulated using our transport model for the HRS with the septum magnet. The first excited state at

3.84 MeV has a cross section that is 0.94% of the elastic cross section, and the placement of the detector suppresses this to a 0.19% background. The next most important contribution is the second excited state at 4.51 MeV, contributing 0.18% background. Altogether, the first ten inelastic states of  $^{48}\text{Ca}$  produce a 0.4% background. This might be further reduced with fine-tuning of the spectrometer optics and detector geometry. The ground state for the  $^{40}\text{Ca}$  isotope contaminant is  $J^\pi = 0^+$  and the asymmetry should be reliably calculable; the first excited state at 3.4 MeV is also  $0^+$  and is mostly suppressed by the HRS.

Based on refs. [59–62], a simple order-of-magnitude estimate for the e-Nucleus asymmetry can be obtained at forward angle where the axial-hadronic contributions to the asymmetry are suppressed both kinematically as well as by the smallness of  $[1 - 4 \sin^2 \theta_W]$ ,

$$A \approx +(-) \frac{G_F Q^2}{4\pi\alpha\sqrt{2}}. \quad (10)$$

Here “+” is for an isoscalar transition and “−” is for isovector. We have made the following cross-checks of eq. (10). We find agreement within a few percent with the Feinberg’s formula [63] for the asymmetry for elastic scattering from  $^{12}\text{C}$ , and a similarly good agreement at forward angle with the asymmetry from the lowest isovector excited state of  $^{12}\text{C}$  at 15.1 MeV calculated in refs. [60,64]. Next, eq. (10) agrees within a factor of 2 with Horowitz’s result [28] for the  $3^-$  state of  $^{208}\text{Pb}$ , mentioned above, as well as if that state were assumed to be isovector.

We believe the low-lying states, as well as elastic scattering, should be predominantly isoscalar. Therefore, the asymmetries are not expected to be significantly different from the measured asymmetry. More accurate calculations of the asymmetry for the isotopes and for low-lying states of  $^{48}\text{Ca}$  would be helpful. The inelastic contamination will also be measured during the experiment using the standard detectors in counting mode.

### 3.5 $Q^2$ measurement

A measurement of  $Q^2$  to better than 1% is needed in order to interpret the asymmetry and extract neutron densities, because the asymmetry is a strong function of  $Q^2$ . For example, for  $^{208}\text{Pb}$  the sensitivity is  $dA_{PV}/dQ^2 \approx 30$  ppm/GeV $^2$  at the kinematics of PREX.

Measuring the small scattering angle is the primary challenge. Survey techniques, while being a good cross-check, are insufficient to constrain the propagated uncertainty to less than 1%. A nuclear recoil technique using a water cell target [22–27, 54, 65] limits the scale error on  $\langle Q^2 \rangle$  to 1%. By comparing the energy difference between the elastically scattered electrons from the protons in water to the elastic peak from  $^{16}\text{O}$  and other heavy nuclei in the water target, the absolute angle can be fixed. This technique was used for PREX and obtained an absolute angle determination of about 0.4 mrad [54]. Anticipating

a comparable energy resolution and the kinematic differences to CREX, an angular determination of 0.28 mrad is expected.

### 3.6 Asymmetry analysis

The result of analysis is an asymmetry at a particular kinematic point. The data used to compute the asymmetry must pass loose requirements on beam quality, but no helicity-dependent cuts are applied. The integrated response for the detectors,  $D$ , and for each beam monitor is digitized and recorded for each helicity window. Denoting beam current as  $I$ , the scattered flux is  $F = D/I$ . For each quartet  $i$ , consisting of helicity windows  $k = 1 - 4$  of 8.23 ms duration, the raw electron cross-section asymmetry  $A_i^{\text{raw}}$  in each HRS is computed from the  $F_k$

$$A_i^{\text{raw}} = \text{sign}_1 \times \left( \frac{F_1 - F_2 - F_3 + F_4}{\sum_k F_k} \right), \quad (11)$$

where  $\text{sign}_1 = \pm$  is the sign of the first window in the helicity pattern (+ - -+) or (- + +-). In addition to quadruplets at 120 Hz, the other patterns tried were octets at 240 Hz and pairs at 60 Hz. As the frequency increases, one expects the uncanceled portion of 60 Hz line  $\sigma_{\text{line}}$  to contribute more to the noise, while the statistical width  $\sigma_{\text{stat}}$  increases. Ideally,  $\sigma_{\text{line}} \ll \sigma_{\text{stat}}$  in a window. Higher frequency also costs statistics because for each helicity flip there is a fixed deadtime (typ. 0.5 ms) to wait for the helicity electronics to settle. The 120 Hz flip rate was chosen to be a reasonable tradeoff. If the beam current and other beam parameters such as position and energy are stable, and if the electronics noise is well suppressed, then the statistical uncertainty is dominated by  $\sigma_{\text{stat}}$  via the detector signals  $D$ .

Random fluctuations in beam position and energy contributed the largest source of noise beyond counting statistics in  $A_{\text{raw}}$ . For PREX-I, typical beam jitter in window quadruplets was less than 700 parts per million (ppm) in intensity, 2 parts per million (ppm) in energy, and 20  $\mu\text{m}$  in position. The intensity noise was removed through normalization to the measured beam intensity, while noise from the other beam parameters was reduced by measuring window differences  $\Delta x_i$  using beam position monitors and applying a correction  $A_{\text{beam}} = \sum c_i \Delta x_i$ . This formula is used both to remove stochastic noise from the beam and to evaluate helicity-correlated corrections. The  $c_i$ 's were measured several times each hour from calibration data in which the beam was modulated by using steering coils and an accelerating cavity. During PREX-I, the largest of the  $c_i$ 's was  $\sim 50$  ppm/ $\mu\text{m}$ . Details of the corrections can be found in refs. [54–58]. The sensitivities for CREX will be smaller because the cross section for  $^{48}\text{Ca}$  drops less rapidly with angle than for  $^{208}\text{Pb}$ .

For PREX-I, the noise in the resulting  $A_{\text{corr}} = A_{\text{raw}} - A_{\text{beam}}$  was 210 (180) ppm per quadruplet, for a beam current of 50 (70)  $\mu\text{A}$ , dominated by counting statistics ( $\sim 1$  GHz at 70  $\mu\text{A}$ ), see fig. 2.

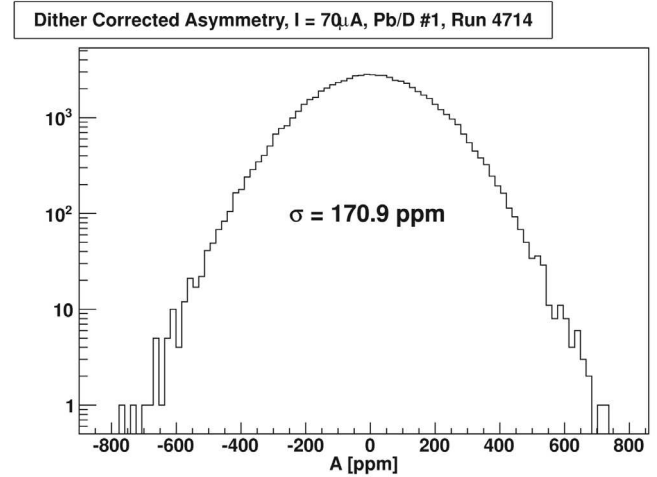


**Fig. 2.** Distribution of the asymmetries for a typical PREX-I run at 70  $\mu\text{A}$ . Beam-related noise has been subtracted using the standard “dither correction” method. The width of 171 ppm is approximately consistent with counting statistics.

**Table 1.** PREX-I corrections to  $A_{PV}$  and systematic errors. See eq. (12) and the discussion below it.

Correction	Absolute (ppb)	Relative (%)
Chg Norm.	$-84.0 \pm 1.5$	$-12.8 \pm 0.2$
Beam Asy	$39.0 \pm 7.2$	$5.9 \pm 1.1$
Target Backing	$-8.8 \pm 2.6$	$-1.3 \pm 0.4$
Detector Nonlin.	$0 \pm 7.6$	$0 \pm 1.2$
Transverse Asy	$0 \pm 1.2$	$0 \pm 0.2$
Polarization $P_b$	$70.9 \pm 8.3$	$10.8 \pm 1.3$
Total	$17.1 \pm 13.7$	$2.6 \pm 2.1\%$

The physics asymmetry  $A_{PV}$  is formed from  $A_{\text{corr}}$  by correcting for the beam polarization  $P_b$  and background fractions  $f_i$  with asymmetries  $A_i$ ,

$$A_{PV} = \frac{1}{P_b} \frac{A_{\text{corr}} - P_b \sum_i A_i f_i}{1 - \sum_i f_i}. \quad (12)$$

The PREX-I corrections are shown in table 1. The corrections are for charge normalization, beam asymmetries, the  $^{12}\text{C}$  backing on the lead target, detector nonlinearities, transverse asymmetries, and beam polarization. The total systematic uncertainty was 2.1% and met the goals of the experiment.

To compare data to theory, we require a spectrometer acceptance function  $\epsilon(\theta)$  which characterizes the probability, as a function of scattering angle  $\theta$ , for an electron to reach the detector after elastically scattering from  $^{208}\text{Pb}$ . For example, the asymmetry averaged over the acceptance would be

$$\langle A \rangle = \frac{\int d\theta \sin \theta A(\theta) \frac{d\sigma}{d\Omega} \epsilon(\theta)}{\int d\theta \sin \theta \frac{d\sigma}{d\Omega} \epsilon(\theta)}, \quad (13)$$

where  $\frac{d\sigma}{d\Omega}$  is the cross section.

Using tracking data, the observed distribution of events corrected for the cross section, backgrounds, and

the effects of multiple scattering is used to extract  $\epsilon(\theta)$ . To compare the experimental asymmetry to predictions, one must integrate the theoretical asymmetry over  $\epsilon(\theta)$ .

### 3.7 Transverse asymmetries

A routine and mandatory part of a parity-violation experiment is to spend about a day measuring the parity-conserving transverse asymmetry  $A_T$  in order to constrain the systematic error from a possible small transverse component of the beam polarization. The measurement of the  $A_T$  itself provides an interesting challenge for theoretical prediction, requiring calculation of box diagrams with intermediate excited states [66, 67].

For these ancillary measurements, the beam polarization is set normal to the nominal electron scattering plane and the asymmetry follows an azimuthal modulation,

$$A_T = A_n \mathbf{P} \cdot \hat{k}, \quad (14)$$

where  $A_T$  is the transverse asymmetry,  $A_n$  is the amplitude of the asymmetry modulation,  $\mathbf{P}$  is the polarization vector of the electron, and  $\hat{k}$  is the unit vector of the cross-product between the incoming and outgoing electron momentum vectors. This asymmetry is a direct probe to the imaginary part of the multiple-photon exchange as it vanishes in the Born approximation by time reversal symmetry. The importance of understanding two-photon exchange has been highlighted by the discrepancy between  $G_E^p$  measurements using Rosenbluth-separation and polarization observables [68], attributable to the real part of the multiple-photon exchange amplitude.

Theoretical predictions are challenging to calculate due to the contributions from hadronic intermediate states in  $\gamma$ - $\gamma$  box diagrams and Coulomb distortion effects which are present for large  $Z$ . However, predictions have been made that these are on the order of a few ppm with beam energies of 1–2 GeV and  $\theta_e \sim$  few degrees using the optical theorem with photoabsorption data [66] to describe the intermediate states. Different approaches, such as using generalized parton distributions to describe  $e-p$  data [69], have also been taken.

Data for these asymmetries with  $^1\text{H}$ ,  $^4\text{He}$ ,  $^{12}\text{C}$ , and  $^{208}\text{Pb}$  have been published [67] and are shown in fig. 3. There is significant disagreement from theory in  $^{208}\text{Pb}$ , the sources of which are not presently well understood and motivate more measurements at intermediate  $Z$ , as well as new calculations that involve simultaneously Coulomb distortions and dispersion corrections. In light of this motivation, the CREX experiment measurements on  $^{48}\text{Ca}$  could be useful to help elucidate the dependence of these asymmetries on  $Z$  and  $Q^2$  by providing an additional data point. Because this asymmetry is so small, directly measuring it requires PV-type precision for which this experiment is designed. A precision of  $\sim 0.5$  ppm would be on similar grounds as the previous data and could be performed in about 1 day.

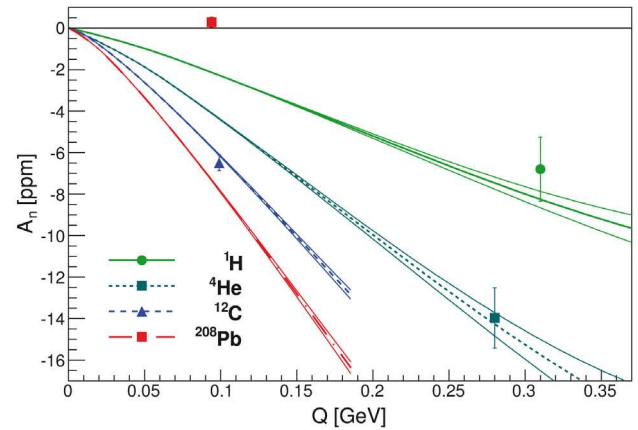


**Fig. 3.** Extracted transverse asymmetries  $A_n$  versus  $Q$  for several different nuclei [67].

### 3.8 Beam polarimetry

Since the beam polarization  $P_b$  is a normalizing factor in the asymmetry, it must be measured with a high precision ( $\frac{dP_b}{P_b} \leq 1\%$ ). Developments in beam polarimetry are of vital importance to the experimental program at Jefferson Lab and are ongoing research projects in themselves. Online monitoring is possible using a Compton polarimeter which is cross-calibrated using Møller and Mott polarimeters. Combining the results of the two polarimeters in Hall A we were able to achieve a better than 1% accuracy in beam polarization during PREX-I [22] and expect incremental improvements in the uncertainties in the next few years.

In recent years, significant upgrades have been performed for the polarimeters. The Hall A Møller polarimeter was upgraded with a stronger magnetic field (3T) to ensure a high polarization of the target foil [70]. In addition, the detectors were segmented and the DAQ upgraded to accommodate higher rates with lower deadtime. The Compton polarimeter was also upgraded prior to PREX-I, in order to achieve an improved figure of merit at low energies by using a new green laser and resonant cavity [71–73]. Using a new DAQ which integrates the signals from back-scattered photons we eliminated the systematic error from thresholds that affected the older counting method. For PREX-I, the total systematic uncertainty contribution from polarimetry totaled 1.2%, a major accomplishment for 1 GeV running. At the 2.2 GeV beam energy of CREX, the Compton Polarimeter will operate with a higher statistical figure of merit and increased resolution of the scattered photon spectrum. The Compton polarimeter results for the HAPPEX-III experiment [71], with a relative systematic error of 0.9% at 3.4 GeV, are a guide for expected systematic errors during CREX. For HAPPEX-III, the systematic error was dominated by a 0.8% uncertainty in laser polarization. New techniques for the control of this uncertainty have been developed during the Qweak experiment [74, 75]. These will be applied in Hall A and can be expected to reduce the photon polarization uncertainty to the level of 0.2%.

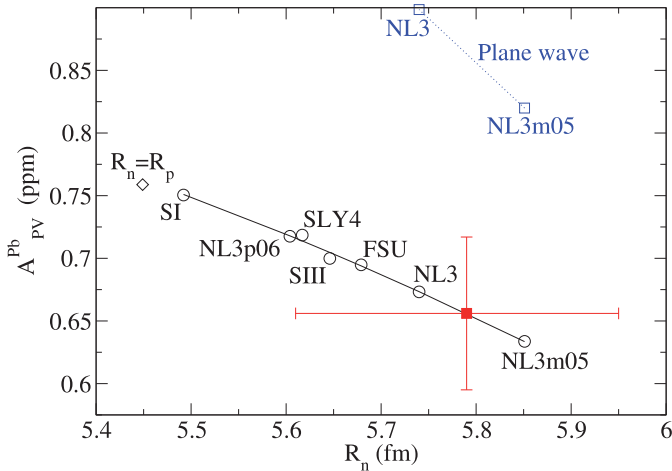


**Fig. 4.** Result of the PREX-I experiment (red square) versus neutron point radius  $R_n$  in  $^{208}\text{Pb}$ . Distorted-wave calculations for seven mean-field neutron densities are circles while the diamond marks the expectation for  $R_n = R_p$  [76]. References: NL3m05, NL3, and NL3p06 from [77], FSU from [78], SIII from [79], SLY4 from [80], SI from [81]. The blue squares show plane wave impulse approximation results.

#### 4 PREX-I result and PREX-II motivation

The “Lead Radius Experiment” PREX first ran in 2010 (PREX-I) and demonstrated successful control of systematic errors, overcoming many technical challenges, but encountered significant loss of beam time due to difficulties with vacuum degradation of the target region due to the high-radiation environment [22]. PREX-II is an approved experiment for a followup measurement with anticipated improvements to take data at a rate equivalent to the original proposal estimates [30]. PREX measures the parity-violating asymmetry  $A_{PV}$  for 1.06 GeV electrons scattered by about five degrees from  $^{208}\text{Pb}$ . A major achievement of PREX-I, despite downtimes mentioned above, was control of the systematic error in  $A_{PV}$  at the 2% level, see table 1 and eq. (12) and the discussion below it.

The result from PREX-I was [22]

$$A_{PV} = 0.656 \pm 0.060(\text{stat}) \pm 0.014(\text{syst}) \text{ ppm.} \quad (15)$$

This result is displayed in fig. 4, in which models predicting the point-neutron radius illustrate the correlation of  $A_{PV}^{\text{Pb}}$  and  $R_n$  [76]. For this figure, seven nonrelativistic and relativistic mean-field models [77–81] were chosen that have charge densities and binding energies in good agreement with experiment, and that span a large range in  $R_n$ . The weak charge density  $\rho_w$  was calculated from model point proton  $\rho_p$  and neutron  $\rho_n$  densities,  $\rho_w(r) = q_p \rho_{ch}(r) + q_n \int d^3r' [G_E^p \rho_n + G_E^n \rho_p]$ , using proton  $q_p = 0.0721$  and neutron  $q_n = -0.9878$  weak charges that include radiative corrections. Here  $G_E^p$  ( $G_E^n$ ) is the Fourier transform of the proton (neutron) electric form factor. The Dirac equation was solved [34] for an electron scattering from  $\rho_w$  and the experimental  $\rho_{ch}$  [4], and the resulting  $A_{PV}(\theta)$  integrated over the acceptance, eq. (13), to yield

the open circles in fig. 4. The importance of Coulomb distortions is emphasized by indicating results from plane-wave calculations, which are not all contained within the vertical axis range of the figure.

From eq. (15), a number of physical quantities were deduced [22,29]. The form factor  $F_W(q)$  of the weak charge density  $\rho_w(r)$  for  $^{208}\text{Pb}$  is (see eq. (4))

$$F_W(q = 0.475 \text{ fm}^{-1}) = 0.204 \pm 0.028. \quad (16)$$

Here the total weak charge of  $^{208}\text{Pb}$  is  $Q_W$  and  $q$  is the momentum transfer of the experiment. The weak radius of  $^{208}\text{Pb}$  (RMS radius of  $\rho_w(r)$ ) is

$$R_W = 5.826 \pm 0.181(\text{exp}) \pm 0.027(\text{mod}) \text{ fm.} \quad (17)$$

Here the experimental error includes both statistical and systematic effects while the small model error includes model uncertainties related to the surface thickness. One needs to make very modest assumptions about the surface thickness in order to extract the RMS radius from a single measurement at the particular  $Q^2$  chosen for the experiment. Comparing eq. (17) to the well-measured charge radius  $R_{ch} = 5.503 \text{ fm}$  yields a “weak charge skin”

$$R_W - R_{ch} = 0.323 \pm 0.181(\text{exp}) \pm 0.027(\text{mod}) \text{ fm.} \quad (18)$$

Thus the surface region of  $^{208}\text{Pb}$  is relatively enhanced in weak charges compared to electromagnetic charges. This weak charge skin is closely related to the expected neutron skin, as discussed below. Equation (18), itself, represents an experimental milestone. We now have direct evidence that the weak charge density of a heavy nucleus is more extended than the electromagnetic charge density. Finally the neutron skin thickness, the difference of the point neutron  $R_n^{208}$  and proton  $R_p^{208}$  radii of  $^{208}\text{Pb}$ , was deduced to be

$$R_n^{208} - R_p^{208} = 0.33_{-0.18}^{+0.16} \text{ fm.} \quad (19)$$

This is a (1.8 $\sigma$ ) observation of the neutron skin in a heavy nucleus with a purely electroweak reaction. PREX-II will have a proposed error in  $R_n^{208}$  smaller by a factor of three to  $\pm 0.06 \text{ fm}$ .

To illuminate the importance of the measurement of  $R_n$  in nuclear matter, we review some of the implications of the proposed PREX-II measurement of neutron radius in  $^{208}\text{Pb}$ . The correlation between  $R_n^{208}$  and the radius of a neutron star,  $r_{NS}$ , has been shown in models to be very strong [82–84]. In general, a larger  $R_n$  implies a stiffer EOS, with a larger pressure, that correlates to larger  $r_{NS}$  [85]. Recently there has been great progress in deducing  $r_{NS}$  from X-ray observations. The value of  $r_{NS}$  is deduced from the spectrum and intensity of the X-rays, with model-dependent corrections for the properties of the atmosphere of the neutron star. The state of the art is as follows. From observations of X-ray bursts from three-ideal neutron stars, Ozel *et al.* [86] find  $r_{NS}$  is very small, near 10 km, implying that the EOS softens at high density which is suggestive of a transition to an exotic phase of QCD. In contrast, Steiner *et al.* [87], using the same three neutron stars plus six more, conclude that  $r_{NS}$  is near 12 km, leading to a prediction that

$R_n^{208} - R_p^{208} = 0.15 \pm 0.02$  fm. This implies a stiffer EOS which leaves little room for softening due to a phase transition at high density.

The EOS of neutron-rich matter is closely related to the symmetry energy  $S$ . There is an empirical strong correlation between  $R_n^{208}$  and the density dependence of the symmetry energy  $dS/d\rho$ , with  $\rho$  as the baryon density, often defined as the parameter  $L = 3\rho(dS/d\rho)$ . Data from a wide variety of nuclear reactions are being used to constrain  $S$  and  $L$ . For example, they can be probed in heavy-ion collisions [88];  $L$  has been extracted from isospin diffusion data [89] using a transport model.

The symmetry energy  $S$  is an important parameter when evaluating the composition and structure of a neutron star. A large  $S$  at high density would imply a large proton fraction, which would allow the direct Urca process ( $n \rightarrow p + e + \bar{\nu}_e$ ;  $p + e \rightarrow n + \nu_e$ ) [90] for rapid neutrino cooling. If  $R_n^{208} - R_p^{208}$  were large, it is likely that massive neutron stars would cool quickly by direct Urca. In addition, the transition density from a solid neutron star crust to the liquid interior is strongly correlated with  $R_n^{208} - R_p^{208}$  [91].

## 5 CREX proposal

The  $^{48}\text{Ca}$  Radius EXperiment (CREX) was recently approved by the program advisory committee at Jefferson Lab [31]. The experiment plans to measure the parity-violating asymmetry for elastic scattering from  $^{48}\text{Ca}$  at  $E = 2.2$  GeV and  $\theta = 4^\circ$ . This will provide a measurement of the weak charge distribution and hence the neutron density at one value of  $Q^2 = 0.022$  (GeV/c) $^2$ . It will provide an accuracy in the  $^{48}\text{Ca}$  neutron radius  $R_n^{48}$  equivalent to  $\pm 0.02$  fm ( $\sim 0.6\%$ ). As discussed below in sects. 5.1 and 5.2, a measurement this precise will have a significant impact on nuclear theory, providing unique experimental input to help bridge *ab initio* theoretical approaches (based on nucleon-nucleon and three-nucleon forces) and the nuclear density functional theory (based on energy density functionals). Together with the PREX measurement of  $R_n^{208}$ , CREX ( $R_n^{48}$ ) will provide unique input in such diverse areas such as neutron star structure, heavy-ion collisions, and atomic parity violation. A precise measurement on a small nucleus is favorable because it can be measured at high momentum transfer where the asymmetry is larger (for the proposed kinematics, about 2 ppm). Also, since  $^{48}\text{Ca}$  is neutron rich it has a relatively large weak charge and greater sensitivity to  $R_n$ .

### 5.1 Testing density functional theory

At the heart of nuclear Density Functional Theory (DFT) calculations [92–94] is an energy density functional whose minimization yields the exact ground-state energy and density of a nucleus. However, DFT does not provide a practical way to compute the functional. The commonly used EDFs are assumed to have a convenient form in terms of local nucleonic densities  $\rho_p(r)$  and  $\rho_n(r)$  and associated currents, involving perhaps a dozen free parameters,

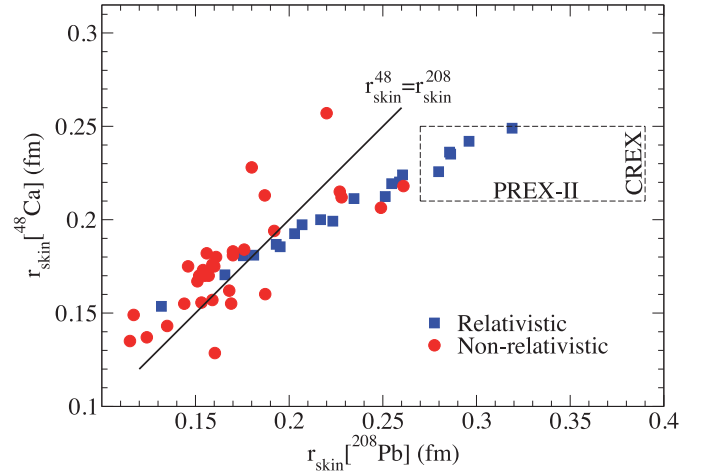


**Fig. 5.** Neutron skin thickness in  $^{48}\text{Ca}$  versus skin thickness in  $^{208}\text{Pb}$  showing predictions for several relativistic (blue squares) and nonrelativistic (red circles) density functionals [31, 100]. Also shown is an error box ( $\pm$  the expected error bars) for CREX and PREX-II. This is located at the PREX-I central value for  $^{208}\text{Pb}$  and at an arbitrary  $^{48}\text{Ca}$  skin thickness.

and these parameters are optimized [95, 96] to reproduce many nuclear observables. Using basic observables of stable nuclei, such as binding energies and charge radii, the optimization accurately constrains how the functional depends on the isoscalar density  $\rho_0(r) = \rho_p(r) + \rho_n(r)$  and its gradient  $\nabla\rho_0(r)$ .

However, there are not many well-measured isovector observables to accurately constrain how the functional depends on the isovector density  $\rho_1(r) = \rho_n(r) - \rho_p(r)$  and  $\nabla\rho_1(r)$ . Isovector fields predicted by various functionals differ [97, 98]; hence, the predicted values for the neutron skin vary significantly. Remarkably, whereas all the available DFT models predict accurately the binding energy and charge radii throughout the nuclear chart, they are unable to agree on whether  $^{48}\text{Ca}$  or  $^{208}\text{Pb}$  has the larger neutron skin [99]. In fig. 5 we show several relativistic and nonrelativistic density functional predictions for the neutron skins in  $^{48}\text{Ca}$  and  $^{208}\text{Pb}$ . These models predict a range of  $^{48}\text{Ca}$  neutron skins that is about seven times larger than the 0.02 fm expected CREX error bar. In contrast the range in predicted  $^{208}\text{Pb}$  skins is only about 3.5 times the expected 0.06 fm PREX II error bar. This suggests that CREX may be particularly helpful in constraining density functionals.

The approved PREX-II measurement of  $R_{\text{skin}}^{208}$ , while relevant for astrophysics, does not fully constrain the isovector sector of the nuclear density functional. PREX-II is critical in constraining the poorly known density dependence of the symmetry energy, particularly the parameter  $L$  that represents the slope of the symmetry energy at saturation density. There is a very strong correlation between  $L$  and  $R_{\text{skin}}^{208}$ , so at present models with different values of  $L$  predict a large range of neutron skins in  $^{208}\text{Pb}$ , ranging from less than 0.1 to greater than 0.3 fm [99]. Thus, even the more accurate PREX-II experiment may be unable to significantly constraint the isovector sector of the nuclear density functional.

However, once  $L$  is constrained by PREX-II, DFT predicts a correlation between  $R_{\text{skin}}^{48}$  and  $R_{\text{skin}}^{208}$  that is testable with CREX, see [94]. For example, a large value of  $R_{\text{skin}}^{208}$  and a small value of  $R_{\text{skin}}^{48}$  is not expected with present EDF parameterizations. If PREX-II and CREX were to yield such results, it would strongly suggest that present density functionals incorrectly model isovector contributions to the nuclear surface energy (for example, gradient terms involving  $\nabla\rho_1(r)$ ). These surface terms are much more important for  $^{48}\text{Ca}$  than for  $^{208}\text{Pb}$  because  $^{48}\text{Ca}$  has a larger ratio of surface to volume. An additional attractive feature of  $^{48}\text{Ca}$ , as compared to  $^{208}\text{Pb}$ , is that the role of electromagnetic effects due to the Coulomb interaction is much reduced in the former system, thus allowing a cleaner study of nuclear isovector properties.

We emphasize that PREX-II and CREX together will constrain isovector contributions to the nuclear EDF. If PREX-II and CREX results agree with DFT expectations, this provides confidence in theoretical predictions of isovector properties all across the periodic table. Apart from the inherent importance for nuclear structure physics, these predictions are important both for atomic parity experiments and for the extrapolation to very neutron-rich systems encountered in astrophysics.

On the other hand, if PREX-II and CREX results disagree with DFT expectations, this will demonstrate that present parameterizations of the isovector part of energy functionals are incomplete. The current parameterizations are prone to large statistical and systematic errors related to isovector terms [98, 101, 102]. Locating and correcting this error is absolutely essential to develop the universal nuclear EDF that will be capable of extrapolating to very neutron-rich nuclei and bulk neutron-rich matter.

## 5.2 *Ab initio* coupled-cluster calculations for $^{48}\text{Ca}$

It is important to have a deeper understanding of energy functionals and to relate DFT results to underlying 2N and 3N interactions. Recently there has been considerable progress in *ab initio* coupled-cluster calculations for medium-mass nuclei [103]. Hagen *et al.* [104] have studied neutron-rich calcium isotopes with large-scale coupled-cluster calculations that take advantage of recent computational advances. These calculations provide a good description of ground and low-lying excited states for a range of calcium isotopes [105].

The effects of 3N forces on the neutron density is significant [106–108]. Therefore a measurement of  $R_{\text{skin}}^{48}$  will provide a very useful test of *ab initio* theory. Present theoretical uncertainties on the  $R_{\text{skin}}^{48}$  prediction are large and include contributions from truncating the chiral expansion, the parameters of the 3N force, model space truncations in many-body calculations, and omitted terms in the coupled-cluster expansion. However the situation is improving rapidly as uncertainty quantification for nuclear structure calculations is an important subject that is receiving considerable attention [109, 110]. For example, More *et al.* have developed ways to minimize errors in calculated radii from model space truncations [111]. We

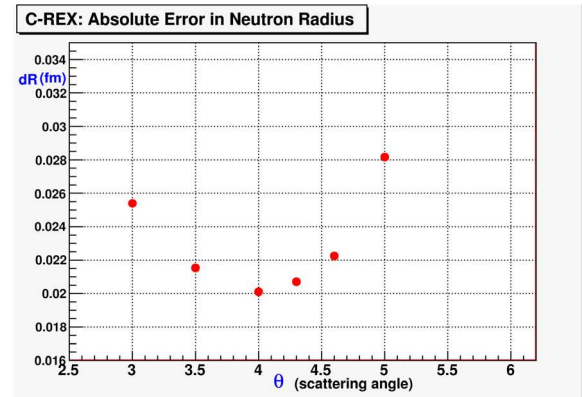


**Fig. 6.** Error in  $R_n$  versus central angle for 2.2 GeV (1-pass beam) for 35 days at  $150\ \mu\text{A}$  for a target thickness of 5% radiation length. Maximizing the FOM (see eq. (9)) minimizes the error in  $R_n$ . A 1.2% systematic error was assumed (see table 3) and added in quadrature to the statistical error. A total error of 0.02 fm is feasible. The optimal angle is  $4^\circ$ .

**Table 2.** Parameters of the PREX (I and II) and CREX experiments.

	PREX	CREX
Energy	1.0 GeV	2.2 GeV
Angle	5 degrees	4 degrees
$A_{PV}$	0.6 ppm	2 ppm
1st Ex. State	2.60 MeV	3.84 MeV
beam current	$70\ \mu\text{A}$	$150\ \mu\text{A}$
Rate	1 GHz	100 MHz
Run time	35 days	45 days
$A_{PV}$ precision	9% (PREX-I) 3% (PREX-II)	2.4%
Error in $R_N$	0.06 fm (PREX-II)	0.02 fm

**Table 3.** Systematic error contributions in CREX.

$Q^2$	0.8%
Polarization	0.8%
Charge Normalization	0.1%
Beam Asymmetries	0.3%
Detector Nonlinearity	0.3%
Transverse	0.1%
Inelastic Contribution	0.2%
Total	1.2%

expect accurate estimations from these *ab initio* calculations in the near future.

Note that at this time we do not yet have accurate calculations of  $R_{\text{skin}}^{48}$  with and without three neutron forces. We expect the skin to be sensitive to three-neutron forces because the pressure of neutron matter was shown to be sensitive to three-neutron forces and the neutron skin in  $^{208}\text{Pb}$  is strongly correlated with the pressure of neutron matter. Therefore it is very important to perform these three-neutron force calculations for  $^{48}\text{Ca}$ .

If CREX agrees with the results of coupled-cluster calculations this provides a crucial test of *ab initio* nuclear structure theory that increases confidence in a variety of nuclear structure predictions and illuminates the role of three-nucleon and in particular three-neutron forces. This is important for a variety of medium-mass neutron-rich isotopes that are presently being studied with radioactive beams. It may also be important for calculations of double-beta-decay matrix elements. (The isotope  $^{48}\text{Ca}$  is the lightest nucleus that undergoes double-beta-decay and we expect microscopic calculations of double-beta-decay matrix elements to be available first for  $^{48}\text{Ca}$ .)

In contrast, if CREX disagrees with these microscopic calculations, something is likely missing from present *ab initio* approaches. For example, the chiral expansion may not converge as well as hoped because of large  $\Delta$  resonance contributions. This would significantly impact all nuclear structure theory.

### 5.3 CREX experiment configuration

The significant new apparatus elements for CREX are the  $^{48}\text{Ca}$  target and a new  $4^\circ$  septum magnet. The rest of the apparatus is standard equipment and the methods of sect. 3 are applied. The experiment is designed for  $150\ \mu\text{A}$  and a  $2.2\ \text{GeV}$  beam energy, which is a natural beam energy at Jefferson Lab (2-passes through the accelerator). At this energy, the figure of merit, which is the total error in  $R_n$  including systematic error, optimizes at a scattering angle of  $4^\circ$ , see fig. 6. Table 2 highlights the experimental configuration and goals of PREX and CREX.

The calcium target will be a  $1\ \text{gm}/\text{cm}^2$  isotopically pure  $^{48}\text{Ca}$  target housed in a vacuum chamber with thin entrance and exit windows. Electrons that scatter from the windows are blocked (energy-degraded) so that they do not reach the detectors.

The total systematic error goal is 1.2% on the asymmetry (see table 3) and the anticipated statistical accuracy is 2.4%. The dominant contributions will be from the  $Q^2$  determination (see subsect. 3.5) and the polarization measurement (subsect. 3.8). These systematic error contributions are all from effects which have been understood and documented by HAPPEX [23–27] and PREX [22, 31, 54–58].

## 6 Conclusions

In this paper we discussed the future measurements PREX-II and CREX at Jefferson Lab. The parity-violating electron scattering asymmetry from  $^{208}\text{Pb}$  and  $^{48}\text{Ca}$  provide a clean measurement at one  $Q^2$  of the weak charge of these nuclei and are sensitive to the nuclear symmetry energy. The experiments leverage the advantages Jefferson Lab, with its highly stable and precisely controlled electron beam and the high-resolution spectrometers, which are uniquely suited to perform these experiments. Within the next few years, these  $R_n$  measurements on  $^{208}\text{Pb}$  and  $^{48}\text{Ca}$  will provide powerful experimental inputs to tune nuclear models of increasing sophistication.

PREX-I achieved the first electroweak observation, at the  $1.8\sigma$  level, of the neutron skin of  $^{208}\text{Pb}$  and successfully demonstrated this technique for measuring neutron densities, with an excellent control of systematic errors. The future PREX-II run will reduce the uncertainty by a factor of three, to  $\pm 0.06\ \text{fm}$  in  $R_n$ . While PREX-II will put a constraint on the density dependence of the symmetry energy (the parameter  $L$ ), models predicting neutron radii of medium-mass and light nuclei are affected by nuclear dynamics beyond  $L$ . CREX will provide new and unique input into the isovector sector of nuclear theories, and the high-precision measurement of  $R_n$  ( $\pm 0.02\ \text{fm}$ ) in a doubly magic nucleus with 48 nucleons will help build a critical bridge between *ab initio* approaches and nuclear DFT. CREX results can be directly compared to new coupled-cluster calculations sensitive to three-neutron forces.

The authors gratefully acknowledge all the collaborators on the PREX-II [30] and CREX [31] proposals and the participants at the CREX 2013 workshop [32], and especially the discussions with G. Hagen, J. Mammey, D. McNulty, W. Nazarewicz, K. Paschke, J. Piekarewicz, S. Riordan, and P.A. Souder. This work was supported by the U.S. Department of Energy, grants DE-FG02-88R40415-A018 (University of Massachusetts) and DE-FG02-87ER40365 (Indiana University), and by the Jefferson Science Associates, LLC, which operates Jefferson Lab for the U.S. DOE under U.S. DOE contract DE-AC05-06OR23177.

## References

1. X. Roca-Maza *et al.*, arXiv:1307.3879 [nucl-th].
2. X. Roca-Maza *et al.*, Phys. Rev. Lett. **106**, 252501 (2011).
3. X. Vinas, M. Centelles, X. Roca-Maza, M. Warda, *Density dependence of the symmetry energy from neutron skin thickness in finite nuclei*, arXiv:1308.1008 [nucl-th], contribution to this Topical Issue.
4. B. Frois *et al.*, Phys. Rev. Lett. **38**, 152 (1977).
5. H. De Vries *et al.*, At. Nucl. Data Tables **36**, 495 (1987).
6. I. Angelia, K.P. Marinova, At. Nucl. Data Tables **99**, 69 (2013).
7. C. Garcia-Recio, J. Nieves, E. Oset, Nucl. Phys. A **547**, 473 (1992).
8. L. Ray, W.R. Coker, G.W. Hoffmann, Phys. Rev. C **18**, 2641 (1978).
9. V.E. Starodubsky, N.M. Hintz, Phys. Rev. C **49**, 2118 (1994).
10. B.C. Clark, L.J. Kerr, S. Hama, Phys. Rev. C **67**, 054605 (2003).
11. A. Trzcinska *et al.*, Phys. Rev. Lett. **87**, 082501 (2001).
12. H. Lenske, Hyperfine Interact. **194**, 277 (2009).
13. A.M. Bernstein, W.A. Seidler, Phys. Lett. B **39**, 583 (1972).
14. A.M. Bernstein, W.A. Seidler, Phys. Lett. B **34**, 569 (1971).
15. A. Krasznahorkay *et al.*, Phys. Rev. Lett. **82**, 3216 (1999).
16. A. Krasznahorkay *et al.*, Nucl. Phys. A **371**, 224 (2004).
17. J. Piekarewicz, *Symmetry energy constraints from giant resonances: A relativistic mean-field theory overview*, arXiv:1307.7746 [nucl-th], contribution to this Topical Issue.

18. M. Warda, X. Vinas, X. Roca-Maza, M. Centelles, Phys. Rev. C **80**, 024316 (2009).
19. P. Danielewicz, Nucl. Phys. A **727**, 233 (2003).
20. Kelly Patton, Jonathan Engel, Gail C. McLaughlin, Nicolas Schunck, Phys. Rev. C **86**, 024612 (2012).
21. C.J. Horowitz, K.J. Coakley, D.N. McKinsey, Phys. Rev. D **68**, 023005 (2003).
22. S. Abrahamyan *et al.*, Phys. Rev. Lett. **108**, 112502 (2012).
23. K.A. Aniol *et al.*, Phys. Rev. Lett. **82**, 1096 (1999).
24. K.A. Aniol *et al.*, Phys. Rev. C **69**, 065501 (2004).
25. K.A. Aniol *et al.*, Phys. Rev. Lett. **96**, 022003 (2006).
26. K.A. Aniol *et al.*, Phys. Rev. Lett. **98**, 032301 (2007).
27. Z. Ahmed *et al.*, Phys. Rev. Lett. **108**, 102001 (2012).
28. C.J. Horowitz, S.J. Pollock, P.A. Souder, R. Michaels, Phys. Rev. C **63**, 025501 (2001).
29. C.J. Horowitz *et al.*, Phys. Rev. C **85**, 032501 (2012).
30. The PREX-II proposal, unpublished, available at [hallaweb.jlab.org/parity/prex](http://hallaweb.jlab.org/parity/prex).
31. The CREX proposal, unpublished, available at [hallaweb.jlab.org/parity/prex](http://hallaweb.jlab.org/parity/prex).
32. <http://www.jlab.org/conferences/crex/>.
33. T.W. Donnelly, J. Dubach, I. Sick, Nucl. Phys. A **503**, 589 (1989).
34. C.J. Horowitz, Phys. Rev. C **57**, 3430 (1998).
35. J. Erler, A. Kurylov, M.J. Ramsey-Musolf, Phys. Rev. D **68**, 016006 (2003).
36. Particle Data Group (K. Nakamura *et al.*), J. Phys. G **37**, 075021 (2010).
37. R.D. McKeown, Phys. Lett. B **219**, 140 (1989).
38. D.T. Spayde *et al.*, Phys. Lett. B **583**, 79 (2004).
39. T. Ito *et al.*, Phys. Rev. Lett. **92**, 102003 (2004).
40. D.H. Beck, Phys. Rev. D **39**, 3248 (1989).
41. D.S. Armstrong *et al.*, Phys. Rev. Lett. **95**, 092001 (2005).
42. D. Androic *et al.*, Phys. Rev. Lett. **104**, 012001 (2010).
43. F.E. Maas *et al.*, Phys. Rev. Lett. **93**, 022002 (2004).
44. F.E. Maas *et al.*, Phys. Rev. Lett. **94**, 152001 (2005).
45. S. Baunack *et al.*, Phys. Rev. Lett. **102**, 151803 (2009).
46. J. Alcorn *et al.*, Nucl. Instrum. Methods A **522**, 294 (2004).
47. C.K. Sinclair *et al.*, Phys. Rev. ST Accel. Beams **10**, 023501 (2007).
48. P.A. Adderley *et al.*, Phys. Rev. ST Accel. Beams **13**, 010101 (2010).
49. J.E. Wise *et al.*, Phys. Rev. C **31**, 1699 (1985).
50. J.M. Cavedon *et al.*, Phys. Rev. Lett. **58**, 195 (1987).
51. H.J. Emrich *et al.*, Nucl. Phys. A **396**, 401C (1983).
52. E.N.M. Quint *et al.*, Phys. Rev. Lett. **57**, 186 (1986).
53. T.B. Humensky, R. Alley, A. Brachmann, M.J. Browne, J. Clendenin, J. deLamare, J. Frisch, T. Galetto *et al.*, Nucl. Instrum. Methods A **521**, 261 (2004).
54. Kiadtisak Saenboonruang, PhD Thesis, University of Virginia (2012) unpublished.
55. Rupesh Silwal, PhD Thesis, University of Virginia (2012) unpublished.
56. Luis R. Mercado, PhD Thesis, University of Massachusetts (2012) unpublished.
57. Chun-Min Jen, PhD Thesis, Syracuse University (2012) unpublished.
58. Zafar Ahmed, PhD Thesis, Syracuse University (2012) unpublished.
59. J.D. Walecka, Nucl. Phys. A **285**, 349 (1977).
60. T.W. Donnelly, R.D. Peccei, Phys. Rep. **50**, 1 (1979).
61. T.W. Donnelly, J.D. Walecka, Annu. Rev. Nucl. Part. Sci. **25**, 329 (1975).
62. T.W. Donnelly, W.C. Haxton, At. Data Nucl. Data Tables **23**, 103 (1979).
63. G. Feinberg, Phys. Rev. D **12**, 3575 (1975) (the sign of the asymmetry in this paper is incorrect).
64. J.S. O'Connell, T.W. Donnelly, J.D. Walecka, Phys. Rev. C **6**, 719 (1972).
65. Technical reports on  $Q^2$  determination at <http://hallaweb.jlab.org/parity/prex/qsq>.
66. M. Gorchtein, C.J. Horowitz, Phys. Rev. C **77**, 044606 (2008).
67. S. Abrahamyan *et al.*, Phys. Rev. Lett. **109**, 192501 (2012).
68. C.F. Perdrisat, V. Punjabi, M. Vanderhaeghen, Prog. Part. Nucl. Phys. **59**, 694 (2007).
69. A.V. Afanasev, S.J. Brodsky, C.E. Carlson, Y.-C. Chen, M. Vanderhaeghen, Phys. Rev. D **72**, 013008 (2005).
70. M. Hauger *et al.*, Nucl. Instrum. Methods A **462**, 382 (2001).
71. M. Friend *et al.*, Nucl. Instrum. Methods A **676**, 96 (2012).
72. Abdurahim Rakhim, PhD Thesis, Syracuse University (2012) unpublished.
73. Megan Friend, PhD Thesis, Carnegie Mellon (2012) unpublished.
74. JLab proposal E02-020, *The Qweak Experiment*, arXiv:1202.1255 [physics.ins-det].
75. Qweak Collaboration (D. Androic *et al.*), Phys. Rev. Lett. **111**, 141803 (2013).
76. S. Ban, C.J. Horowitz, R. Michaels, J. Phys. G **39**, 015104 (2012).
77. G.A. Lalazissis, J. König, P. Ring, Phys. Rev. C **55**, 540 (1997).
78. B.G. Todd-Rutel, J. Piekarewicz, Phys. Rev. Lett. **95**, 122501 (2005).
79. M. Beiner, H. Flocard, N. Van Giai, P. Quentin, Nucl. Phys. A **238**, 29 (1975).
80. E. Chabanat, P. Bonche, P. Haensel, J. Meyer, R. Schaer, Nucl. Phys. A **635**, 231 (1998).
81. D. Vautherin, D.M. Brink, Phys. Rev. C **5**, 626 (1972).
82. C.J. Horowitz, J. Piekarewicz, Phys. Rev. C **64**, 062802 (2001).
83. S. Gandolfi, J. Carlson, Sanjay Reddy, Phys. Rev. C **85**, 032801 (2012).
84. J. Erler *et al.*, arXiv:1211.6292 [nucl-th].
85. A.W. Steiner, J.M. Lattimer, E.F. Brown, Astrophys. J. **765**, L5 (2013).
86. F. Ozel, G. Baym, T. Guver, Phys. Rev. D **82**, 101301 (2010).
87. A.W. Steiner, J.M. Lattimer, E.F. Brown, Astrophys. J. **722**, 33 (2010).
88. W.G. Lynch, M.B. Tsang, Y. Zhang, P. Danielewicz, M. Famiano, Z. Li, A.W. Steiner, arXiv:0901.0412.
89. M.B. Tsang, Yingxun Zhang, P. Danielewicz, M. Famiano, Zhuxia Li, W.G. Lynch, A.W. Steiner, Phys. Rev. Lett. **102**, 122701 (2009).
90. C.J. Horowitz, J. Piekarewicz, Phys. Rev. C **66**, 055803 (2002).

91. C.J. Horowitz, J. Piekarewicz, Phys. Rev. Lett. **86**, 5647 (2001).
92. M. Bender, P.-H. Heenen, P.-G. Reinhard, Phys. Rev. Mod. **75**, 121 (2003).
93. W. Nazarewicz, P.-G. Reinhard, W. Satula, D. Vretenar, *Symmetry energy in nuclear density functional theory*, arXiv:1307.5782 [nucl-th], contribution to this Topical Issue.
94. P.-G. Reinhard *et al.*, arXiv:1308.1659 [nucl-th].
95. M. Kortelainen *et al.*, Phys. Rev. C **77**, 064307 (2008).
96. M. Kortelainen *et al.*, Phys. Rev. C **82**, 024313 (2010).
97. J. Piekarewicz *et al.*, Phys. Rev. C **85**, 041302 (2012).
98. J. Erler, N. Birge, M. Kortelainen, W. Nazarewicz, E. Olsen, A.M. Perhac, M. Stoitsov, Nature **486**, 509 (2012).
99. J. Piekarewicz, contribution to the CREX 2013 workshop, in preparation.
100. J. Piekarewicz, private communication.
101. P.G. Reinhard, W. Nazarewicz, Phys. Rev. C **81**, 051303 (2010).
102. Y. Gao, J. Dobaczewski, M. Kortelainen, J. Toivanen, D. Tarpanov, Phys. Rev. C **87**, 034324 (2013).
103. C. Forssén, G. Hagen, M. Hjorth-Jensen, W. Nazarewicz, J. Rotureau, Phys. Scr. T **152**, 014022 (2013).
104. G. Hagen *et al.*, Phys. Rev. Lett. **109**, 032502 (2012).
105. A.T. Gallant *et al.*, Phys. Rev. Lett. **109**, 032506 (2012).
106. J.D. Holt *et al.*, J. Phys. G **39**, 085111 (2012).
107. K. Hebeler, R.J. Furnstahl, Phys. Rev. C **87**, 031302 (2013).
108. I. Tews, T. Krueger, K. Hebeler, A. Schwenk, Phys. Rev. Lett. **110**, 032504 (2013).
109. S. Bogner *et al.*, Comput. Phys. Commun. (2013).
110. A. Ekström, G. Baardsen, C. Forssén, G. Hagen, M. Hjorth-Jensen, G.R. Jansen, R. Machleidt, W. Nazarewicz, T. Papenbrock, J. Sarich, S.M. Wild, Phys. Rev. Lett. **110**, 192502 (2013).
111. S.N. More, A. Ekstrom, R.J. Furnstahl, G. Hagen, T. Papenbrock *et al.*, Phys. Rev. C **87**, 044326 (2013).